RSC Advances

PAPER

View Article Online
View Journal | View Issue

Cite this: *RSC Adv.*, 2025, **15**, 19741

High thermal stability and tensile-strength bacterial cellulose–silica–PEO composite solid polymer electrolyte for long-life and dendrite-free lithium metal batteries†

Hwichan Hong, ‡[a] Seungman Park,‡[a] Seon Jae Hwang,[a] Minjun Bae, [a] Yonghwan Kim, [a] Won Young An,[a] Yongyeol Park,[a] Dohyeong Kim, [a] Yujin Chang[a] and Yuanzhe Piao *[ab]

The increasing demand for high-energy-density and safe energy storage systems has driven the advancement of solid-state lithium metal batteries (LMBs). However, conventional liquid electrolytes face serious challenges such as dendrite growth, low thermal stability, and flammability, which limit their practical application. Solid polymer electrolytes (SPEs) have emerged as promising alternatives due to their improved safety and flexibility, but they still suffer from low ionic conductivity and insufficient mechanical and thermal robustness. In this study, we report a novel SPE composed of SiO_2-coated bacterial cellulose and polyethylene oxide (BC/PEO@SiO_2), synthesized *via* a facile and cost-effective sol–gel method. The incorporation of SiO_2-coated BC nanofibers significantly enhanced the composite's mechanical strength and thermal resistance, achieving a nearly sevenfold increase in tensile strength compared to neat PEO. Moreover, the membrane maintained its structural integrity even at 150 °C. Electrochemical testing confirmed the excellent performance of the BC/PEO@SiO_2 as a SPE. The Li|BC/PEO@SiO_2|Li symmetric cell maintained stable lithium plating and stripping behavior for over 700 hours, indicating superior interfacial stability. Furthermore, the LFP|BC/PEO@SiO_2|Li full cell exhibited a high reversible capacity of 113 mA h g^{-1} and retained 94% of its initial capacity after 200 cycles. These results demonstrate that BC/PEO@SiO_2 is a promising and scalable SPE platform for next-generation, safe and high-performance solid-state lithium batteries.

Received 30th March 2025
Accepted 4th June 2025

DOI: 10.1039/d5ra02218e

rsc.li/rsc-advances

1. Introduction

The growing demand for high-capacity energy storage solutions, such as electric vehicles (EV) and large-scale energy storage systems (EES), has driven the rapid development of next-generation battery technologies.[1–4] Lithium metal batteries (LMBs) have emerged as strong candidates to replace conventional lithium-ion batteries (LIBs), due to their extremely low electrochemical potential (−3.04 V *vs.* SHE) and high theoretical specific capacity (3860 mA h g^{-1}).[5–7] However, the use of conventional liquid electrolytes in LMBs poses serious challenges, including the growth of lithium dendrites, poor thermal and electrochemical stability, and the risk of flammability, all of which hinder their practical adoption.[8–11]

Solid-state electrolytes (SSEs) have attracted attention as promising alternatives to liquid electrolytes, offering improved safety, mechanical strength, and chemical stability.[12–14] SSEs can be broadly classified into three types: inorganic, polymer-based (SPEs), and hybrid electrolytes. Inorganic SSEs, such as sulfide- and oxide-based materials, offer high ionic conductivity and thermal stability.[15,16] However, their application is restricted by brittleness and poor interfacial compatibility.[17] Notably, sulfide-based electrolytes like LPSCl have been reported to undergo thermal runaway at relatively low temperatures due to reactions with delithiated cathodes,[18] while oxide-based materials like LATP also exhibit instability at the lithium interface.[19,20]

In contrast, solid polymer electrolytes (SPEs) offer advantages such as excellent processability, flexibility, thin-film formability, and good interfacial compatibility with electrodes.[21–23] However, their practical application is hindered by inherently low ionic conductivity, limited mechanical robustness, and poor thermal stability.[24,25] Therefore, there is a growing need to engineer SPEs

[a]*Graduate School of Convergence Science and Technology, Seoul National University, 145 Gwanggyo-ro, Yeongtong-gu, Suwon-Si, Gyeonggi-do, 16229, Republic of Korea. E-mail: parkat9@snu.ac.kr*

[b]*Advanced Institutes of Convergence Technology, 145 Gwanggyo-ro, Yeongtong-gu, Suwon-si, Gyeonggi-do, 16229, Republic of Korea*

† Electronic supplementary information (ESI) available. See DOI: https://doi.org/10.1039/d5ra02218e

‡ These authors contributed equally to this work.

that simultaneously enhance mechanical strength, ionic conductivity, and thermal stability. Among various SPEs, polyethylene oxide (PEO) is considered one of the most promising polymer hosts due to its good flexibility, electrochemical stability, and strong coordination with lithium ions.[26–28] However, the high crystallinity of PEO at room temperature significantly limits ion mobility, resulting in low ionic conductivity ($<10^{-5}$ to 10^{-6} S cm^{-1}).[29] Moreover, its poor mechanical strength, narrow electrochemical window (<4 V *vs.* Li/Li$^+$), and decreased performance and structure decomposition at elevated temperatures hinder its practical applications.[30,31] To overcome these limitations, extensive efforts have been made to incorporate inorganic or organic fillers—such as SiO_2,[32,33] Al_2O_3,[34] TiO_2,[35] or metal–organic frameworks (MOFs)[36]—into the PEO matrix. These fillers are known to reduce PEO crystallinity, form continuous Li$^+$ conduction pathways, and improve mechanical and thermal stability of the electrolyte.

Cellulose-based materials have been investigated as functional components in SPEs due to their abundance, biodegradability, and outstanding mechanical characteristics.[37–39] Among them, bacterial cellulose (BC) stands out owing to its high purity, nanofiber structure, large surface area, and high aspect ratio. These features make BC an ideal filler for reinforcing solid polymer electrolytes.[40,41] Although the incorporation of bacterial cellulose (BC) into PEO improves the mechanical properties of the solid polymer electrolyte, the composite still suffers from several limitations.[42] The lack of lithium-ion conduction pathways in BC results in low ionic conductivity. Furthermore, the poor interfacial contact with lithium metal and potential aggregation of BC nanofibers may deteriorate the electrochemical performance and cycling stability.[43] The SiO_2 coating on bacterial cellulose mitigates fiber aggregation and promotes uniform dispersion within the polymer matrix.[44] Furthermore, it substantially improves both the thermal stability and mechanical strength of the resulting composite electrolyte.[45,46] In addition, the SiO_2 coating reduces the crystallinity of polyethylene oxide (PEO), facilitating the formation of a more amorphous phase that favors lithium-ion transport, thereby improving ionic conductivity.[47–49]

In this work, we introduce a surface-modified strategy by coating bacterial cellulose (BC) nanofibers with SiO_2 *via* a facile sol–gel method. The synthesized SiO_2-coated bacterial cellulose–polyethylene oxide (BC/PEO@SiO_2) composite exhibits a significantly improved tensile strength of 4.12 MPa, compared to the pure PEO electrolyte, which shows only 0.62 MPa. Moreover, the BC/PEO@SiO_2 membrane retains its structural integrity even at elevated temperatures up to 150 °C, indicating excellent thermal stability. Li‖BC/PEO@SiO_2‖Li symmetric cells demonstrate stable lithium plating/stripping behavior for over 700 hours at 60 °C under varying current densities from 0.05 to 0.4 mA cm^{-2}. In addition, LFP‖BC/PEO@SiO_2‖Li full cells deliver a high reversible capacity of 113 mA h g^{-1}, maintaining 94% capacity retention after 200 cycles at 60 °C and 1C. This study not only provides an effective strategy for the development of next-generation, safe, sustainable, and high-performance polymer-based solid-state electrolytes, but also highlights the potential for scalable and economically viable production.

2. Experimental

Materials

Bacterial cellulose (*nata de coco*) was obtained from Vietnam Coco Food Co., Ltd. (Tang Nhon Phu, Vietnam). Ethanol (EtOH), lithium perchlorate (anhydrous, 95%) was purchased from Samchun chemicals. Cetyltrimethylammonium bromide (CTAB), tetraethyl orthosilicate (TEOS) and acetonitrile (anhydrous) was purchased from Sigma-Aldrich. Polyethylene oxide (PEO, Organics, M_w: 600 000) was obtained from Acros Organics.

Preparation of the BC/SiO_2

Nata de coco (1 kg) was soaked in flowing deionized water (DW) for 3 days to remove residual sugars and other impurities. The purified bacterial cellulose (BC) was then physically crushed, divided into 50 mL portions, and stored at 4 °C for further use.

For silica coating, 0.4 g of cetyltrimethylammonium bromide (CTAB) and 25 mL of ethanol (EtOH) were added to a 100 mL vial and stirred until completely dissolved. Subsequently, 50 mL of the prepared BC suspension, 25 mL of DW, and 1 mL of ammonium hydroxide solution were added to the mixture and stirred for 10 minutes. Afterward, 1 0 μL of tetraethyl orthosilicate (TEOS) was added, and the reaction was allowed to proceed overnight under ambient conditions. The resulting product was collected and washed three times with ethanol by centrifugation at 8000 rcf.

Preparation of SiO_2 nanoparticles and BC + SiO_2 NP

SiO_2 nanoparticles were synthesized *via* the Stöber method. 35 mL of DW, 25 mL of EtOH, and 2.5 mL of ammonium hydroxide solution were sequentially added into a 70 mL vial under ambient conditions. Subsequently, 10 mL of TEOS was added dropwise, and the mixture was stirred at 450 rpm at room temperature overnight. The resulting silica nanoparticles were collected by centrifugation at 8000 rcf and washed three times with ethanol to remove residual reagents.

To prepare the BC + SiO_2 NP composite, the as-synthesized SiO_2 nanoparticle dispersion was added to the bacterial cellulose (BC) solution at a ratio of 5 wt% relative to the dry weight of BC. The mixture was stirred for 1 hour to allow uniform dispersion of the nanoparticles within the BC matrix.

Preparation of bare PEO

PEO and lithium perchlorate were dissolved in acetonitrile at an EO : Li-ion ratio of 16 : 1. The solution was then stirred vigorously in an orbital mixer (AR-100, Thinky mixer) to form a homogeneous solution. The solution was drop-cast on a polytetrafluoroethylene (PTFE) dish and dried in a vacuum oven at 60 °C for 48 h to evaporate the solvent.

Preparation of BC@PEO and BC/SiO_2@PEO

BC or BC/SiO_2 film (2 cm by 2 cm) was placed on PTFE dish. A bare PEO solution was drop-cast on the pre-prepared PTFE dish and dried in a vacuum oven at 60 °C for 48 h to evaporate the

solvent. The composition ratios of each component in the composite electrolytes are PEO : BC = 9 : 2 and PEO : BC : SiO_2 = 9 : 2 : 0.1 by weight.

Characterization of the composite

Scanning electron microscopy (SEM) images were obtained with a field emission scanning electron microscope (FE-SEM; Hitachi S-4800, 15 kV) equipped with an energy-dispersive spectrometer (EDS). Nitrogen adsorption/desorption isotherms at 77 K were measured using a BELSORP-mini II (MicrotracBEL Corp.). The microstructures of the samples were characterized by transmission electron microscopy (TEM; JEM1010, 80 kV). Thermogravimetric analysis (TGA), differential thermal analysis (DTA) and differential scanning calorimetry was performed using a simultaneous DTA/TGA analyser (SDT 650, TA instruments) over a temperature range of 25–700 °C with a ramp rate of 10 °C min^{-1} in air. FT-IR measurements were performed on Thermo Scientific FT-IR Spectrophotometer (Nicolet 5700). The crystallographic structures of the samples were characterized by X-ray diffraction (XRD; Bruker D8 Advance, 40 mA, 40 kV, Cu-Kα radiation source, scan range in 2θ of 10–80°). Mechanical properties of PEO based films were examined by an universal test machine TD-U10 (T&DORF, Korea).

Electrochemical measurement

The ionic conductivity was measured by recording the electrochemical impedance spectra (EIS) of stainless steel (SS)/SPE/SS cells using a Zive SP1 (Zive Lab) over a frequency range of 106 Hz to 0.1 Hz, within a temperature range of 30–60 °C. The electrochemical stability windows of the SPEs were evaluated using linear sweep voltammetry (LSV) in a SS/SPE/Li cell configuration at 60 °C, with a scan rate of 1 mV s from 0 V to 6.0 V. A symmetric Li/SPE/Li cell was assembled to evaluate the interfacial stability and polarization behavior under elevated current densities. To prepare the $LiFePO_4$ cathode, commercial $LiFePO_4$ powder, poly(vinylidene fluoride) (PVDF), and carbon black (Super P) were mixed in a weight ratio of 8 : 1 : 1 using *N*-methyl-2-pyrrolidone (NMP) as the solvent. The mixture was ball-milled to obtain a homogeneous slurry, which was then cast onto aluminum foil using a doctor blade. The electrode was subsequently dried in a vacuum oven at 60 °C overnight. The $LiFePO_4$/SPE/Li full cells were assembled by a CR2016 coin-type cell in an argon-filled glove box (O_2 and H_2O < 0.1 ppm). The rate capability and cycling performance were evaluated at various current densities using a WBCS3000S cycler (WonA-Tech, Korea) within a voltage window of 2.0–4.2 V at 60 °C.

3. Results and discussion

As illustrated in the schematic diagram in Fig. 1, commercially available bacterial cellulose (*nata de coco*) was processed into a film-like form and subsequently coated with silica *via* a simple and cost-effective sol–gel method. This approach enabled the facile synthesis of silica-coated bacterial cellulose, which was then incorporated with polyethylene oxide (PEO) to fabricate the BC/SiO_2@PEO solid polymer electrolyte (SPE). Based on this composite, both Li|BC/PEO@SiO_2|Li symmetric cells and LFP|BC/PEO@SiO_2|Li full cells were assembled, and their electrochemical performances were systematically evaluated.

Transmission electron microscopy (TEM) analysis was performed to investigate the morphology and structural characteristics of the BC/SiO_2 composite. As shown in Fig. 2a, the BC nanofibers exhibit a well-defined, entangled fibrous network with uniform diameters, typically ranging below 100 nm. The presence of a distinct, conformal silica layer surrounding the BC fibers is evident, indicating successful surface coating. In addition, the appearance of dark, spherical domains along the fibers suggests the formation of silica nanoparticles, which are likely nucleated and grown on the fiber surface during the sol–gel process.

Fig. S1† presents the cross-sectional SEM image and corresponding EDS elemental mapping of the BC/SiO_2@PEO composite solid polymer electrolyte. Elemental mapping confirms the successful incorporation and distribution of each component within the composite. Carbon (C), primarily originating from the BC matrix and PEO, is uniformly distributed across the cross-section. Oxygen (O) is also uniformly distributed, indicating the coexistence of BC and the SiO_2 framework. Notably, the presence of silicon (Si) signals indicates the successful surface coating of SiO_2 on the BC nanofibers.

The chemical structures and interactions of BC, BC/SiO_2, PEO, and BC/SiO_2@PEO were investigated by Fourier transform infrared (FTIR) spectroscopy in the range of 4000–400 cm^{-1}, as shown in Fig. 2b. All samples exhibited a broad absorption band around 3200–3500 cm^{-1}, corresponding to the O–H stretching vibration, which is characteristic of hydroxyl groups present in cellulose and PEO. In the 2900 cm^{-1} region, a prominent C–H stretching band appeared in the BC/SiO_2@PEO spectra, which is attributed to the methylene groups (–CH_2–) in PEO chains. The absorption peak near 1100 cm^{-1} in the BC/SiO_2 and BC/SiO_2@PEO samples is assigned to the Si–O–Si stretching vibration, indicating the presence of silica networks. Notably, the intensity of this peak is significantly higher in the BC/SiO_2 and BC/SiO_2@PEO samples than in pure BC or PEO, verifying the formation of SiO_2 within the composite. These FTIR results confirm the successful formation of the BC/SiO_2 BC/SiO_2@PEO hybrid structures.

X-ray diffraction (XRD) analysis was conducted to investigate the crystalline structures of PEO, BC/SiO_2, and the hybrid composite BC/SiO_2@PEO. The XRD patterns are presented in Fig. 2c. In the case of BC/SiO_2, several distinct but broader peaks were observed in the 2θ range of 15–30°, indicating the presence of crystalline domains in bacterial cellulose, along with an amorphous halo that can be attributed to the incorporated silica. The partial broadening of peaks compared to pure BC suggests a reduction in crystallinity due to the introduction of SiO_2, which is typically amorphous. The XRD pattern of the BC/SiO_2@PEO hybrid composite revealed a combination of features from both PEO and BC/SiO_2. The characteristic crystalline peaks of PEO were retained, albeit with reduced intensity and slight broadening. This suggests that the incorporation of BC/SiO_2 disrupted the regular packing of PEO chains, leading to a decrease in the overall crystallinity of the hybrid. Additionally,

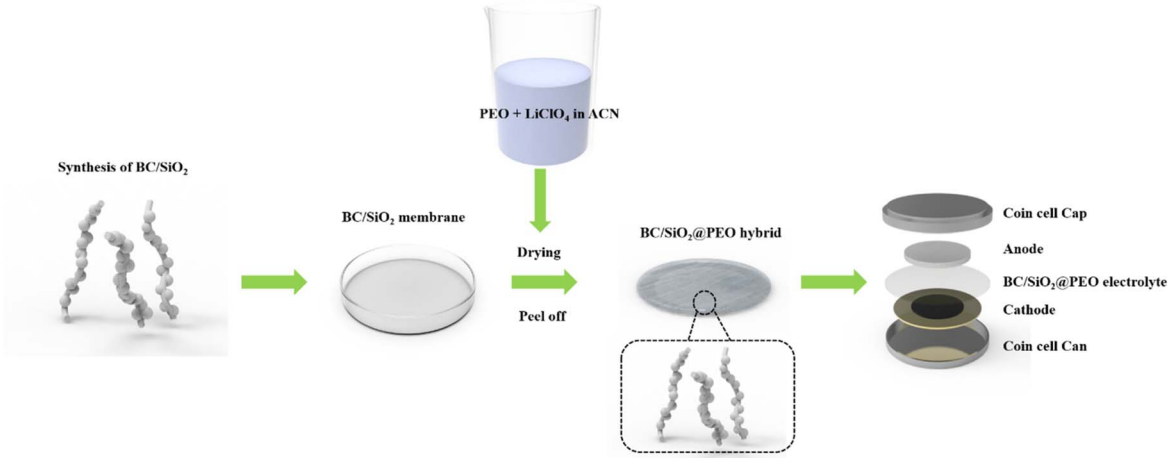

Fig. 1 Schematic diagram of BC/SiO_2@PEO composite synthesis procedure.

the presence of broad humps in the composite pattern further supports the existence of amorphous SiO_2 domains within the matrix. These results indicate successful hybridization of the three components, where PEO chains interact with the BC/SiO_2 network, resulting in a composite material with both crystalline and amorphous characteristics.

X-ray photoelectron spectroscopy (XPS) was employed to analyze the chemical composition and bonding environments of the BC/SiO_2@PEO composite, with particular focus on the C 1s and Si 2p core-level spectra. As shown in Fig. S4,† the high-resolution C 1s spectrum was deconvoluted into two major peaks. The dominant peak at 284.8 eV is assigned to C–C/C–H bonds, which are typical of the cellulose backbone. The secondary peak at ~286.3 eV corresponds to C–O bonds, reflecting the presence of ether linkages from the PEO matrix.

The Si 2p spectrum exhibits a single prominent peak centered at ~102.3 eV, which is characteristic of Si–O bonding in SiO_2. This observation confirms the successful incorporation of silica within the composite. Overall, the XPS results verify the successful integration of all three components—bacterial

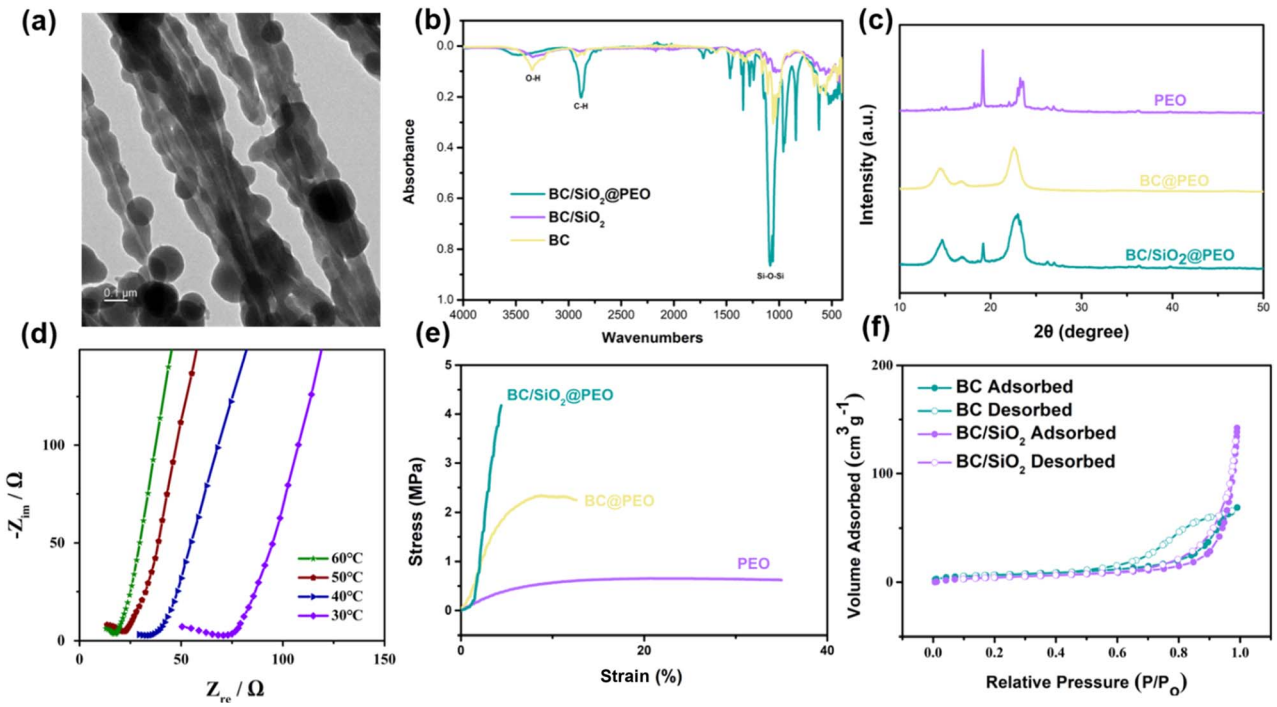

Fig. 2 Morphological and structural characterization of the solid polymer electrolyte. (a) TEM image of BC/SiO_2 nanofibers. (b) FTIR spectra of BC, BC/SiO_2, and BC/SiO_2 composites. (c) XRD patterns of PEO, BC/SiO_2, and BC/SiO_2@PEO composites. (d) Temperature-dependent electrochemical impedance spectra (EIS) of BC/SiO_2@PEO composite electrolyte at different temperatures. (e) Stress–strain curves of PEO, BC@PEO, BC/SiO_2@PEO. (f) Nitrogen adsorption–desorption isotherms (BET) of BC and BC/SiO_2.

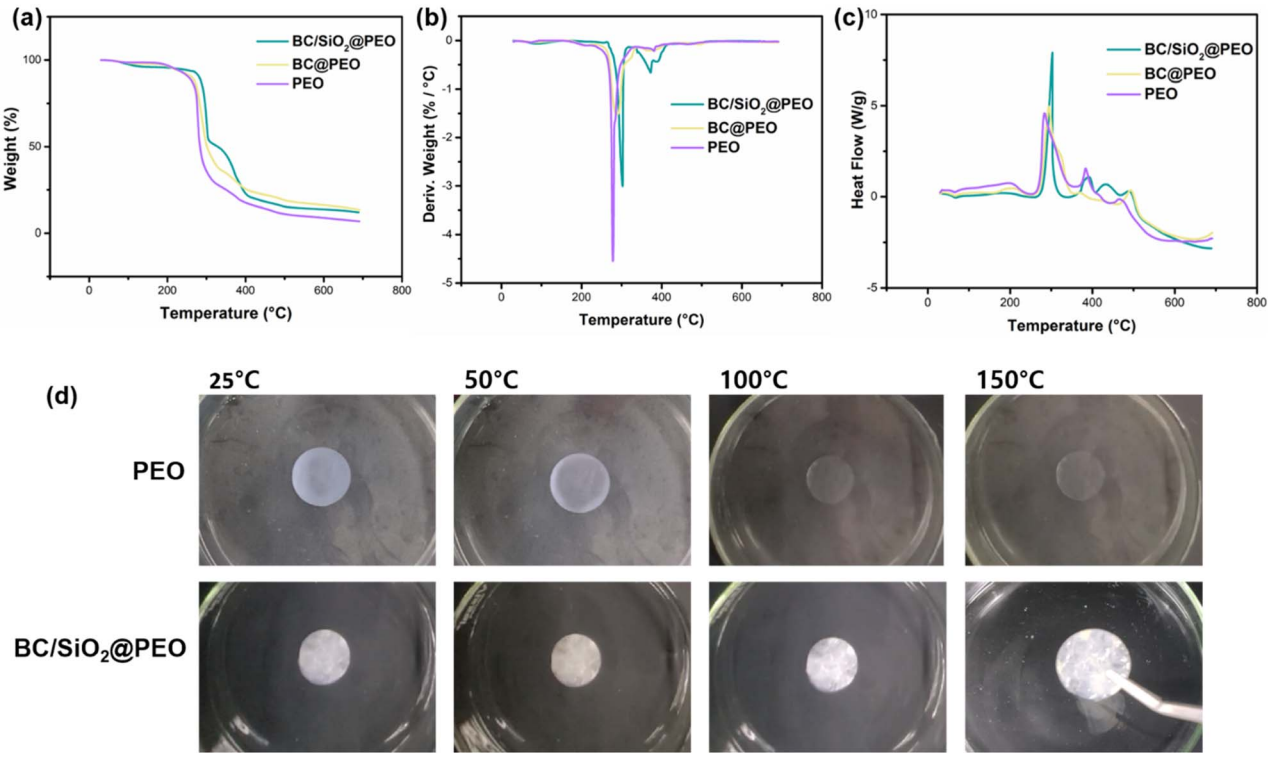

Fig. 3 (a) Thermogravimetric analysis (TGA), (b) differential thermal analysis (DTA), and (c) differential scanning calorimetry (DSC) curves of PEO, BC@PEO, and BC/SiO_2@PEO solid polymer electrolytes. (d) Optical images of the electrolytes at different temperatures (25 °C, 50 °C, 100 °C, and 150 °C).

cellulose, SiO_2, and PEO—into a chemically coherent composite structure.

Electrochemical impedance spectroscopy (EIS) was conducted to evaluate the ionic conductivity of the BC/SiO_2@PEO solid polymer electrolyte at various temperatures, as shown in Fig. 2d. The Nyquist plots exhibit typical semicircular behavior followed by a linear tail, indicating the combined effects of bulk resistance and ion diffusion. As the temperature increases from 30 °C to 60 °C, the diameter of the semicircle decreases significantly, reflecting a reduction in bulk resistance and enhanced ionic conductivity. This temperature-dependent decrease in impedance suggests that ion transport within the BC/SiO_2@PEO matrix is thermally activated.

Linear sweep voltammetry (LSV) was conducted to evaluate the electrochemical stability window of the BC–SiO_2/PEO composite solid electrolyte. As shown in Fig. S2,† the current density remained nearly zero up to approximately 4.2 V *vs.* Li/Li^+, indicating that the electrolyte is electrochemically stable within this potential range. A sharp increase in current density was observed beyond 4.2 V, which is attributed to the onset of oxidative decomposition of the electrolyte. This result suggests that the BC–SiO_2/PEO electrolyte exhibits a wide electrochemical stability window from 0 to 4.2 V.

The mechanical properties of solid polymer electrolytes are critical for their application in solid-state lithium metal batteries. As shown in Fig. 2e, the stress–strain curves of the PEO-based solid polymer electrolytes reveal a substantial improvement in tensile strength upon incorporation of bacterial cellulose (BC) and SiO_2. Specifically, the tensile strength increased approximately fourfold for BC@PEO and nearly sevenfold for BC/SiO_2@PEO, compared to neat PEO. These results demonstrate that the incorporation of SiO_2-coated BC nanofibers provides significant reinforcement of the polymer matrix, leading to enhanced mechanical robustness. Remarkably, despite this notable increase in mechanical strength, the composite electrolyte retained excellent flexibility, as shown in Fig. S3.† The film could be bent or twisted without cracking or delamination, indicating that the mechanical enhancement strategy does not compromise the inherent flexibility of the PEO matrix. This favorable balance between strength and flexibility is crucial for maintaining interfacial integrity and mechanical durability during battery operation.

Fig. 2f presents the N_2 adsorption–desorption isotherms of pristine BC and BC/SiO_2. Compared to BC, the BC/SiO_2 sample exhibited a markedly higher nitrogen uptake over the entire relative pressure range and a clear hysteresis loop, indicating a significant increase in surface area and the development of mesoporous structures as a result of SiO_2 coating.

The thermal stability of the samples was systematically evaluated using thermogravimetric analysis (TGA), differential thermal analysis (DTA), and derivative thermogravimetry (DTG), as shown in Fig. 3a–c.

As presented in Fig. 3a, all samples exhibited two-step thermal degradation behavior. Pristine PEO showed a rapid weight loss beginning near 300 °C, with a significant drop occurring around 370 °C, resulting in a relatively low residual

weight at 700 °C. The incorporation of bacterial cellulose (BC@PEO) delayed the onset of thermal degradation and slightly increased the residual mass, indicating improved thermal stability due to the presence of thermally stable BC nanofibers. Notably, the BC/SiO_2@PEO composite demonstrated the highest thermal resistance, with a further delayed decomposition onset and the largest residual weight, attributed to the thermal buffering effect of inorganic SiO_2 and its ability to hinder polymer chain motion during degradation.

The DTA thermograms in Fig. 3b support these findings by showing a pronounced exothermic peak corresponding to the main decomposition event of PEO near 370 °C. This exothermic peak shifted to slightly higher temperatures for BC@PEO and even further for BC/SiO_2@PEO, indicating delayed decomposition. Additionally, the broadening and intensity change of the peaks suggest altered degradation kinetics and enhanced thermal stability in the composites. The presence of SiO_2 likely introduces thermal inertia and limits heat flow, contributing to the thermal resistance of the hybrid system.

Further insight into the degradation kinetics was obtained through DTG curves, shown in Fig. 3c. Pristine PEO exhibited the sharpest and most intense degradation peak, corresponding to the highest rate of weight loss. BC/PEO displayed a broader, less intense peak, indicating a slower degradation rate. In contrast, BC/SiO_2@PEO showed the most delayed and broadened degradation peak, confirming that the addition of SiO_2 effectively retards the thermal decomposition process and stabilizes the composite structure.

Collectively, the results from TGA, DTA, and DTG analyses consistently demonstrate that the introduction of BC and particularly BC coated with SiO_2 significantly improves the thermal stability of PEO. This enhancement can be attributed to the synergistic effects of the BC matrix and the thermally inert SiO_2, which together reduce the decomposition rate and increase the overall thermal resistance of the composite electrolyte system.

Thermal stability of BC/SiO_2@PEO and PEO SPE are compared at different temperature. In Fig. 3d, no significant morphological difference is observed between PEO and BC/SiO_2@PEO at 25 °C. However, as the temperature increases to 100 °C, the PEO undergoes melting, while the BC–SiO_2-containing composite retains its structural integrity. Even at 150 °C, the BC/SiO_2@PEO electrolyte maintains its morphology without noticeable deformation, whereas the PEO sample exhibits pronounced melting behavior due to its limited thermal stability. This thermal degradation may lead to internal short circuits and potential battery failure at elevated temperatures. These results clearly demonstrate that incorporating BC–SiO_2 significantly enhances the thermal stability of the composite electrolyte.

To further investigate the effect of the silica incorporation method on the structural and mechanical properties of the composite solid polymer electrolytes, SiO_2 nanoparticles with an average diameter of approximately 100 nm—comparable to the coated SiO_2 domains observed in BC/SiO_2 structures—were synthesized (Fig. S5†). These SiO_2 NPs were incorporated into the BC matrix *via* physical mixing to fabricate a BC + SiO_2 NP@PEO composite electrolyte. The resulting films were then systematically characterized using FTIR, XRD, stress–strain analysis, and BET surface area measurements.

In the FTIR spectrum (Fig. S6a†), the BC + SiO_2 NP composite displayed a broad O–H stretching band and a distinct Si–O–Si peak near 1050 cm^{-1}, confirming the presence of silica. However, in comparison to the BC/SiO_2@PEO sample, the peak appeared weaker and broader, indicating less pronounced interfacial interactions between the physically blended nanoparticles and the BC network.

The XRD profile (Fig. S6b†) revealed a reduction in crystallinity relative to pristine BC, yet higher crystallinity than that observed in the BC/SiO_2@PEO composite, suggesting that the physically mixed NPs were less effective in disrupting PEO chain alignment, potentially due to nanoparticle agglomeration. Mechanical testing (Fig. S6c†) demonstrated that the BC + SiO_2 NP@PEO composite possessed a higher tensile strength (~3.8 MPa) than the PEO and BC@PEO samples, validating the reinforcement effect of silica nanoparticles. However, both strength and elongation remained inferior to those of the BC/SiO_2@PEO composite, likely due to the absence of a continuous interfacial network.

To evaluate the porosity and surface area of the physically mixed structure, nitrogen adsorption–desorption isotherm analysis was performed (Fig. S6d†). The BC + SiO_2 NP composite exhibited a type IV isotherm with a hysteresis loop, indicating mesoporous characteristics. Although the specific surface area increased compared to pristine BC, it was still lower than that of the BC/SiO_2-coated structure. This finding indicates that physically dispersed nanoparticles are less efficient than conformally coated SiO_2 in preventing the aggregation of bacterial cellulose nanofibers, which in turn limits the formation of a uniformly porous and interconnected network.

In terms of thermal performance, temperature-dependent morphological analysis up to 150 °C (Fig. S7d†) showed that the BC + SiO_2 NP@PEO film maintained its shape and integrity, similar to the BC/SiO_2@PEO film. Thermogravimetric (TGA), derivative thermogravimetric (DTG), and differential scanning calorimetry (DSC) analyses (Fig. S7a–c†) were also conducted to examine decomposition behavior and phase transitions. The TGA curve revealed a two-step degradation pattern, comparable to BC/SiO_2@PEO, though with a slightly earlier onset of degradation. The DTG curve exhibited a broad degradation peak near 400 °C, indicating less effective thermal shielding relative to the coated counterpart. Likewise, DSC analysis showed broad and less defined melting/crystallization transitions, suggesting partial suppression of PEO crystallinity, yet not to the extent achieved with the coated architecture.

Taken together, these results suggest that while BC + SiO_2 NP@PEO exhibits notable thermal resilience up to 150 °C and contributes to mesoporous structuring and mechanical reinforcement, it falls short of the performance achieved by the BC/SiO_2@PEO composite. Based on these structural, thermal, and mechanical characterizations, it is reasonable to infer that the electrochemical performance of the BC + SiO_2 NP@PEO system may also be inferior to that of the BC/SiO_2@PEO composite. The lack of uniform interfacial contact, limited dispersion of SiO_2

nanoparticles, and reduced structural integration are likely to impede ionic transport and compromise electrode–electrolyte interfacial stability. This comparative analysis clearly demonstrates that conformal SiO_2 coating on BC nanofibers, rather than simple nanoparticle mixing, is more effective in enhancing the physical, thermal properties of the solid polymer electrolyte system.

Overall, while the BC + SiO_2 NP@PEO composite demonstrated marginal improvement over the BC-only system, its performance did not reach the level achieved by the BC/SiO_2@PEO structure. This result highlights the critical role of interfacial architecture and coating uniformity in optimizing the mechanical and structural integrity of solid polymer electrolytes.

The electrochemical stability of the solid polymer electrolytes was evaluated using Li/Li symmetrical cells under various current densities, as shown in Fig. 4a. The PEO-based cell exhibited unstable and fluctuating voltage profiles during the initial cycling at 0.05 mA cm^{-2}, indicating poor interfacial contact and the onset of polarization caused by lithium dendrite formation. Notably, the PEO/$LiCl_4$ SPE cell failed at approximately 65 h as the current density increased, due to the insufficient mechanical strength of the electrolyte.

In contrast, the BC/SiO_2@PEO cell demonstrated a remarkably stable and symmetric voltage response throughout the entire cycling test, even as the current density was gradually increased from 0.05 mA cm^{-2} to 0.4 mA cm^{-2} and then decreased back to 0.1 mA cm^{-2}. This enhanced voltage stability suggests improved ionic conductivity, effective suppression of lithium dendrite growth, and better interfacial compatibility enabled by the incorporation of the BC–SiO_2 framework.

To further investigate the cycling behavior of the BC/SiO_2@PEO electrolyte, enlarged voltage profiles at various time intervals are presented in Fig. 4b–g. As shown in Fig. 4b, the PEO cell exhibited significant voltage fluctuations between 40 and 60 h, whereas the BC/SiO_2@PEO cell maintained a stable overpotential of approximately 20–30 mV under the same conditions. During long-term cycling (Fig. 4c–g), the BC/SiO_2@PEO cell consistently displayed highly stable and repetitive voltage plateaus, with negligible increases in overpotential

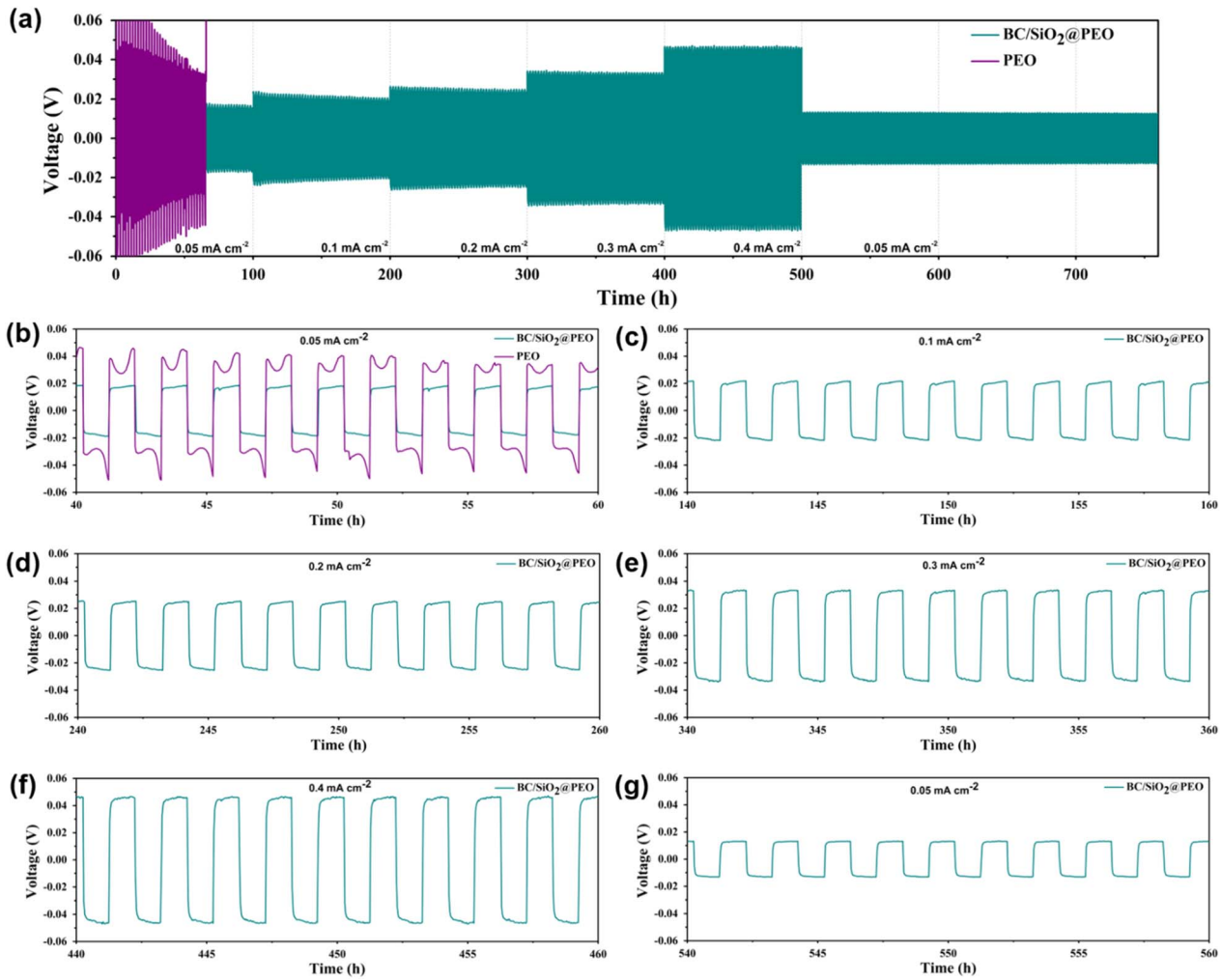

Fig. 4 (a) Voltage profiles showing the rate performance of Li/Li symmetrical cells using PEO–$LiCl_4$ and BC/SiO_2@PEO–$LiCl_4$ solid polymer electrolytes at various current densities. (b–g) Enlarged voltage–time curves of the BC/SiO_2@PEO cell during cycling at different current densities.: (b) 0.05 mA cm^{-2}, (c) 0.1 mA cm^{-2}, (d) 0.2 mA cm^{-2}, (e) 0.3 mA cm^{-2}, (f) 0.4 mA cm^{-2}, and (g) 0.05 mA cm^{-2}.

even after 560 hours. This excellent electrochemical durability highlights the mechanical robustness and efficient lithium-ion transport pathways provided by the composite electrolyte.

Overall, these results clearly demonstrate that the integration of the BC–SiO_2 framework into the PEO matrix not only reinforces the mechanical integrity of the electrolyte but also facilitates uniform lithium plating and stripping, thereby contributing to enhanced safety and extended cycle life in lithium metal batteries.

The electrochemical performance of the BC/SiO_2@PEO was then examined in a full-cell environment, where LFP–Li system was employed for the test. Furthermore, a temperature-dependent galvanostatic cycling was conducted from 10 to 60 °C at a constant rate of 0.2C, with the corresponding voltage profiles at various temperatures presented in Fig. 5a. It is noted that even at a low temperature of 10 °C, a relatively high capacity of ≈100 mA h g^{-1} was retained. Once the temperature is elevated slightly to 30 °C, a much higher specific capacity of ≈135 mA h g^{-1} with low polarization was achieved. An increase in temperature from 40 to 60 °C further boosted the capacity to near theoretical values (theoretical: 170 mA h g^{-1}).

To evaluate performance at higher voltages, pouch cells were subjected to electrochemical testing. As shown in Fig. 5b, the BC/SiO_2@PEO cell demonstrated high discharge capacities of 160, 151, and 141 mA h g^{-1} at 0.05, 0.2, and 0.5C rates, respectively. Notably, upon returning to 0.05C, the discharge capacity recovered to 157 mA h g^{-1}, indicating excellent rate capability and capacity retention. In contrast, the PEO cell exhibited a significantly lower discharge capacity of only 12 mA h g^{-1} at a 0.2C rate and failed to recover its capacity when returned to 0.05C.

The cycling performance of PEO-based solid polymer electrolytes was evaluated in Li–LFP full cells at 1C for 200 cycles, as shown in Fig. 5c. The cell employing pristine PEO exhibited poor electrochemical performance, with a low initial discharge capacity of approximately 30 mA h g^{-1} and continuous capacity fading throughout the cycling process. In contrast, the BC/SiO_2@PEO composite electrolyte demonstrated a significantly improved cycling stability, retaining a specific capacity of ~130 mA h g^{-1} and maintaining 94% of its initial capacity after 200 cycles. This enhanced performance is closely associated with the synergistic role of the BC–SiO_2 framework, which not only improves the thermal and mechanical stability of the composite but also facilitates favorable interfacial interactions with the electrode surface. Specifically, the SiO_2 domains uniformly distributed on the BC nanofibers are rich in hydroxyl

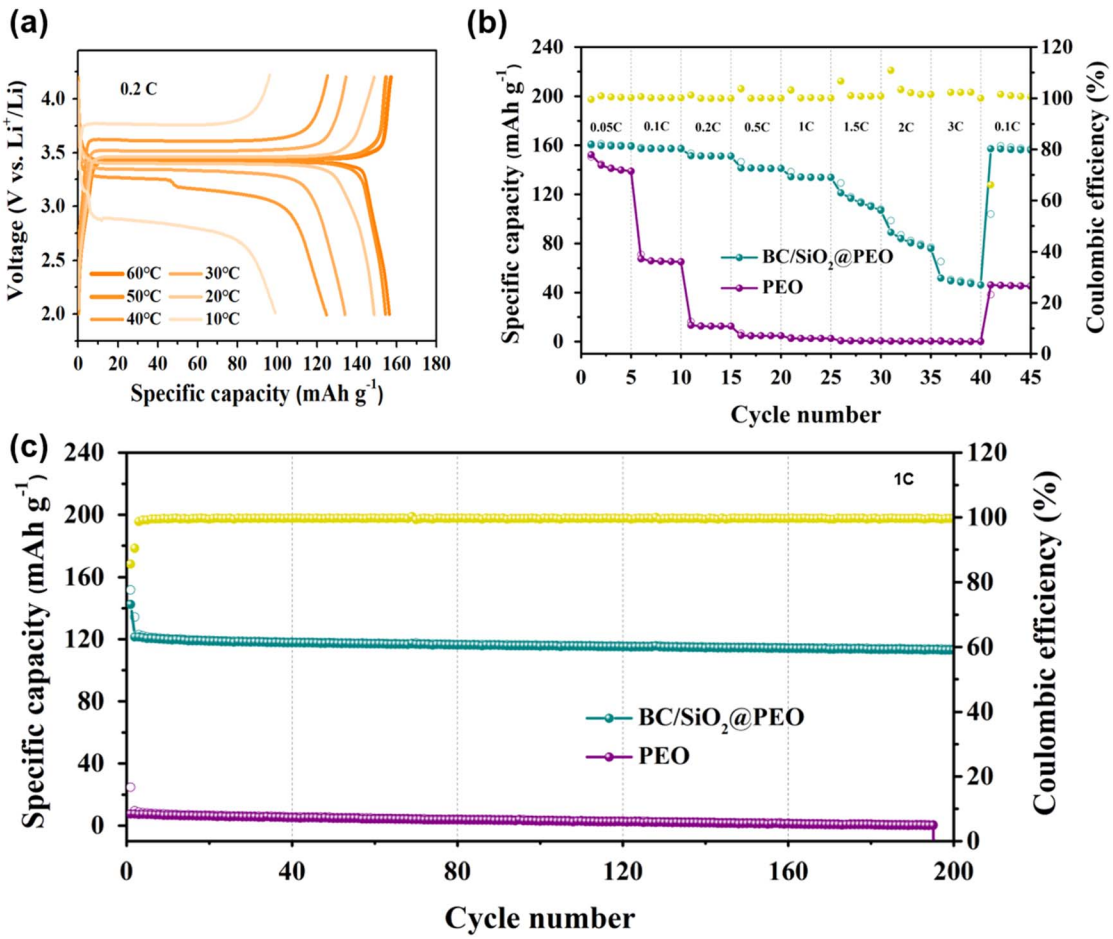

Fig. 5 (a) Voltage profiles of the LFP–Li cells at various temperatures from 10 to 60 °C, where the rate was fixed at 0.2C. (b) The rate capability curves of the batteries at different current densities at 60 °C. (c) Cycling stability (left *y*-axis) of LFP–Li cells with (green) and without (purple) BC–SiO_2 at 60 °C which exhibits stable cycling for at least 200 cycles.

(–OH) groups, which enable hydrogen bonding or Lewis acid–base interactions with anions, thereby promoting Li salt dissociation. These chemical interactions serve as interfacial anchors, improving structural cohesion during cycling. In parallel, the mechanically robust BC–SiO_2 framework effectively suppresses lithium dendrite growth by maintaining a uniform ion flux and distributing mechanical stress across the interface. These results confirm that the incorporation of BC–SiO_2 substantially improves the long-term electrochemical stability of PEO-based solid-state electrolytes in lithium metal batteries.

4. Conclusion

In this study, we developed a novel solid polymer electrolyte (SPE) by incorporating SiO_2-coated bacterial cellulose into a polyethylene oxide (PEO) matrix, forming a BC/SiO_2@PEO composite. This composite was synthesized through a simple and cost-effective sol–gel method, offering advantages in both scalability and material sustainability. Structural and electrochemical characterizations revealed that the introduction of the SiO_2-coated BC network significantly enhanced the mechanical strength—achieving nearly a sevenfold increase in tensile strength—and thermal stability, with the composite maintaining its integrity even at 150 °C. The electrolyte also demonstrated excellent electrochemical performance. The Li|BC/SiO_2@PEO|Li symmetric cell maintained stable lithium plating/stripping behavior for over 700 hours, and the LFP|BC/SiO_2@PEO|Li full cell delivered a reversible discharge capacity of 113 mA h g^{-1} with 94% capacity retention over 200 cycles. These findings confirm that the BC/SiO_2@PEO composite provides a promising pathway toward the development of high-performance and safe SPEs for next-generation solid-state lithium metal batteries. Future research should focus on further improving ionic conductivity and long-term interfacial stability to enable full-scale commercial application.

Data availability

The data supporting this article have been included as part of the ESI.†

Author contributions

Hwichan Hong: conceptualization, methodology, investigation, formal analysis, writing-original draft; Seungman Park: conceptualization, methodology, investigation, formal analysis; Seon Jae Hwang: methodology, formal analysis; Minjun Bae: validation, investigation, writing-review & editing; Yonghwan Kim: validation, investigation, writing-review & editing; Won Young An: investigation, resources; Yongyeol Park: investigation, resources; Dohyeong Kim: investigation, resources; Yujin Chang: investigation, resources.

Conflicts of interest

All authors declared that there are no conflicts of interest.

Acknowledgements

This research was supported by the Basic Science Research Program through the National Research Foundation of Korea (NRF), funded by the Ministry of Education (2023R1A2C2007699 and 2022R1A6A1A03063039), and the Nano Material Technology Development Program through the NRF, funded by the Ministry of Science and ICT (NRF-2015M3A7B6027970). Additionally, support was provided by the Korea Evaluation Institute of Industrial Technology (KEIT) grant funded by the Korea government (MOTIE) (00437804) and the Technology Innovation Program (or Industrial Strategic Technology Development Program) ("RS-2023-00236794", Development of composite powder for high heat dissipation-EMI shielding coating in next-generation semiconductor) funded by the Ministry of Trade, Industry & Energy (MOTIE, Korea) (1415187474).

References

1 J.-M. Tarascon and M. Armand, *Nature*, 2001, **414**, 359–367.
2 P. G. Bruce, B. Scrosati and J. M. Tarascon, *Angew. Chem., Int. Ed.*, 2008, **47**, 2930–2946.
3 J. B. Goodenough and Y. Kim, *Chem. Mater.*, 2010, **22**, 587–603.
4 N. Nitta, F. Wu, J. T. Lee and G. Yushin, *Mater. Today*, 2015, **18**, 252–264.
5 S. Chu and A. Majumdar, *Nature*, 2012, **488**, 294–303.
6 W. Xu, J. Wang, F. Ding, X. Chen, E. Nasybulin, Y. Zhang and J.-G. Zhang, *Energy Environ. Sci.*, 2014, **7**, 513–537.
7 D. Lin, Y. Liu and Y. Cui, *Nat. Nanotechnol.*, 2017, **12**, 194–206.
8 Y. Lu, Z. Tu and L. A. Archer, *Nat. Mater.*, 2014, **13**, 961–969.
9 Z. Hou, J. Zhang, W. Wang, Q. Chen, B. Li and C. Li, *J. Energy Chem.*, 2020, **45**, 7–17.
10 K. Shen, Z. Wang, X. Bi, Y. Ying, D. Zhang, C. Jin, G. Hou, H. Cao, L. Wu and G. Zheng, *Adv. Energy Mater.*, 2019, **9**, 1900260.
11 S. H. Wang, Y. X. Yin, T. T. Zuo, W. Dong, J. Y. Li, J. L. Shi, C. H. Zhang, N. W. Li, C. J. Li and Y. G. Guo, *Adv. Mater.*, 2017, **29**, 1703729.
12 Y. Liu, Q. Liu, L. Xin, Y. Liu, F. Yang, E. A. Stach and J. Xie, *Nat. Energy*, 2017, **2**, 1–10.
13 G. V. Alexander, M. Indu, S. Kamakshy and R. Murugan, *Electrochim. Acta*, 2020, **332**, 135511.
14 X. Shen, X. Cheng, P. Shi, J. Huang, X. Zhang, C. Yan, T. Li and Q. Zhang, *J. Energy Chem.*, 2019, **37**, 29–34.
15 Y. Seino, T. Ota, K. Takada, A. Hayashi and M. Tatsumisago, *Energy Environ. Sci.*, 2014, **7**, 627–631.
16 C. Wang, K. Adair and X. Sun, *Acc. Mater. Res.*, 2021, **3**, 21–32.
17 J. Sun, C. He, Y. Li, Q. Zhang, C. Hou, M. De Volder, K. Li and H. Wang, *Energy Storage Mater.*, 2023, **54**, 40–50.
18 T. Kim, K. Kim, S. Lee, G. Song, M. S. Jung and K. T. Lee, *Chem. Mater.*, 2022, **34**, 9159–9171.
19 R. Chen, A. M. Nolan, J. Lu, J. Wang, X. Yu, Y. Mo, L. Chen, X. Huang and H. Li, *Joule*, 2020, **4**, 812–821.
20 H. Chung and B. Kang, *Chem. Mater.*, 2017, **29**, 8611–8619.

21 Z. Song, F. Chen, M. Martinez-Ibañez, W. Feng, M. Forsyth, Z. Zhou, M. Armand and H. Zhang, *Nat. Commun.*, 2023, **14**, 4884.
22 D. Zhou, D. Shanmukaraj, A. Tkacheva, M. Armand and G. Wang, *Chem*, 2019, **5**, 2326–2352.
23 S. Xu, Z. Sun, C. Sun, F. Li, K. Chen, Z. Zhang, G. Hou, H. M. Cheng and F. Li, *Adv. Funct. Mater.*, 2020, **30**, 2007172.
24 D. Zhang, X. Meng, W. Hou, W. Hu, J. Mo, T. Yang, W. Zhang, Q. Fan, L. Liu and B. Jiang, *Nano Res. Energy*, 2023, **2**, e9120050.
25 Z. Li, J. Fu, X. Zhou, S. Gui, L. Wei, H. Yang, H. Li and X. Guo, *Advanced Science*, 2023, **10**, 2201718.
26 W. Gorecki, M. Jeannin, E. Belorizky, C. Roux and M. Armand, *J. Phys.: Condens. Matter*, 1995, **7**, 6823.
27 D. Zhang, L. Li, X. Wu, J. Wang, Q. Li, K. Pan and J. He, *Front. Energy Res.*, 2021, **9**, 726738.
28 W. Li, Y. Pang, J. Liu, G. Liu, Y. Wang and Y. Xia, *RSC Adv.*, 2017, **7**, 23494–23501.
29 X. Yang, Q. Sun, C. Zhao, X. Gao, K. R. Adair, Y. Liu, J. Luo, X. Lin, J. Liang and H. Huang, *Nano Energy*, 2019, **61**, 567–575.
30 A. Du, H. Lu, S. Liu, S. Chen, Z. Chen, W. Li, J. Song, Q. H. Yang and C. Yang, *Adv. Energy Mater.*, 2024, **14**, 2400808.
31 B. Guo, Y. Fu, J. Wang, Y. Gong, Y. Zhao, K. Yang, S. Zhou, L. Liu, S. Yang and X. Liu, *Chem. Commun.*, 2022, **58**, 8182–8193.
32 Y. Tominaga, S. Asai, M. Sumita, S. Panero and B. Scrosati, *J. Power Sources*, 2005, **146**, 402–406.
33 M.-H. Lee, T. Dam, S.-J. Baek and C.-J. Park, *J. Power Sources*, 2025, **629**, 236130.
34 S. Venkatesan, Y.-Y. Chen, C.-Y. Chien, M.-H. Tsai, H. Teng and Y.-L. Lee, *Electrochim. Acta*, 2021, **380**, 137588.
35 E. Zhao, Y. Guo, A. Zhang, H. Wang and G. Xu, *Nanoscale*, 2022, **14**, 890–897.
36 Z. Zhang, Y. Huang, H. Gao, C. Li, J. Hang and P. Liu, *J. Energy Chem.*, 2021, **60**, 259–271.
37 D. Wang, H. Xie, Q. Liu, K. Mu, Z. Song, W. Xu, L. Tian, C. Zhu and J. Xu, *Angew. Chem., Int. Ed.*, 2023, **62**, e202302767.
38 Y. A. Samad, A. Asghar and R. Hashaikeh, *Renewable Energy*, 2013, **56**, 90–95.
39 Q. Sabrina, C. R. Ratri, A. Hardiansyah, T. Lestariningsih, A. Subhan, A. Rifai, R. Yudianti and H. Uyama, *RSC Adv.*, 2021, **11**, 22929–22936.
40 Z. J. Zheng, H. Ye and Z. P. Guo, *Adv. Mater.*, 2024, 2412908.
41 Y. Zhang, Y. Chen, X. Li, M. Alfred, D. Li, F. Huang and Q. Wei, *J. Power Sources*, 2021, **482**, 228963.
42 Y. Li, Z. Sun, D. Liu, S. Lu, F. Li, G. Gao, M. Zhu, M. Li, Y. Zhang and H. Bu, *Energy Environ. Mater.*, 2021, **4**, 434–443.
43 X. Chen, Y. Huang, L. Zhang, J. Liu, C. Wang and M. Wu, *Carbohydr. Polym.*, 2022, **290**, 119504.
44 D. Liu, Q. Wu, R. L. Andersson, M. S. Hedenqvist, S. Farris and R. T. Olsson, *J. Mater. Chem. A*, 2015, **3**, 15745–15754.
45 S. Hribernik, M. S. Smole, K. S. Kleinschek, M. Bele, J. Jamnik and M. Gaberscek, *Polym. Degrad. Stab.*, 2007, **92**, 1957–1965.
46 J. Liu, P. Chen, D. Qin, S. Jia, C. Jia, L. Li, H. Bian, J. Wei and Z. Shao, *Carbohydr. Polym.*, 2020, **233**, 115818.
47 S. Ketabi and K. Lian, *Electrochim. Acta*, 2013, **103**, 174–178.
48 Z. Shen, Y. Cheng, S. Sun, X. Ke, L. Liu and Z. Shi, *Carbon Energy*, 2021, **3**, 482–508.
49 Y. Jiang, Y. Li, F. Dong, X. Chu, J. Li, H. Xie and J. Liu, *J. Energy Storage*, 2024, **88**, 111558.